



UNIVERSITÉ CATHOLIQUE DE LOUVAIN

Study of the stress relieve heat-treatment of additively manufactured AlSi10Mg alloy:

Influence on microstructure and mechanical properties

Dissertation presented by

David DISPAS

and

Arthur BOUILLOT

for obtaining the Master's degree in

Mechanical Engineering

and

Chemical and Materials
Engineering

at Ecole Polytechnique de Louvain (EPL)

Supervisor: Aude SIMAR

Readers: Laurent DELANNAY, Anne MERTENS, Camille VAN DER REST

Academic year 2017-2018

"The gem cannot be polished without friction, nor man perfected without trials."

Confucius

Acknowledgements

...

Contents

1	Introduction	1
2	State of the art	3
2.1	Selective laser melting technology	3
2.2	AlSi10Mg alloy	5
2.3	Fabrication process parameters	5
2.4	As-built mechanical properties	8
2.5	Post treatments	9
3	Materials and methods	11
3.1	Powder follow-up	11
3.1.1	Sieving	11
3.1.2	Grain size and distribution	11
3.1.3	Composition	11
3.2	Manufacturing parameters	11
3.3	Heat treatments	13
3.4	Characterisation	13
3.4.1	Density	13
	Hydrostatic weighing	13
	Relative optical density image analysis	14
3.4.2	Microstructure	15
	Scanning electron microscopy	15
	Optical microscopy	15
3.4.3	Composition	15
3.4.4	Internal stress	15
3.4.5	Mechanical properties	15
	Hardness test	15
	Tensile tests	16
4	Results	17
4.1	Parameters optimisation	17
4.2	Reproducibility	18
4.2.1	Relative density and hardness	18
	Generalities	18
	Position influence	18
	Proximity influence	18
	Time influence	18
4.2.2	Melt pool size and distribution	18
4.3	Internal properties homogeneity	18
4.4	Powder ageing	19
4.4.1	Grain size and distribution	19
	Fresh powder	19
	Recycled powder	19

4.4.2	Composition	19
	Fresh powder	19
	Recycled powder	19
4.5	Heat treatments	20
4.5.1	Heating process	20
4.5.2	Microscopy	20
4.5.3	Hardness testing	20
4.5.4	Tensile testing	20
4.5.5	Internal stress testing	20
5	Discussion	23
5.1	Parameters optimisation	23
5.2	Reproducibility	23
5.2.1	Melt pool size distribution	23
5.3	Powder ageing	23
5.3.1	Grain size and distribution	23
5.3.2	Composition	23
5.4	Density measures assessments	23
5.4.1	Hydrostatic weighing	23
5.4.2	Relative optical density image analysis	23
5.5	Measures comparison	25
5.6	Heat treatments	25
5.6.1	Heating process??	25
5.6.2	Microstructure	25
5.6.3	Mechanical properties	25
5.6.4	Internal stress	25
5.6.5	Optimisation	25
6	Conclusion	29
A	Batches fabrication details	31
A.1	Process parameters	31
A.2	Specimens positioning, fabrication orders and sintering times	31
A.2.1	Batch X200-171024	31
A.2.2	Batch X200-180109	31
A.2.3	...Other batches	31
B	Extract of Vickers hardness conversion table (HV10)	35
C	Procedure for the confidence intervals computation	37
C.1	Hydrostatic weighting	37
C.2	Vickers hardness	37
	Bibliography	39

List of Figures

2.1 Selective laser melting technology principle	3
2.2 (a)Research publications on SLM of ceramics, composites and all materials types combined. (b)Research publications on SLM of different metallic materials	4
2.3 Parameters involved in SLM	5
2.4 Process window for SLM of AlSi10Mg, based on the top view of single track scans	6
2.5 Process window for SLM of AlSi10Mg, based on the front view of single track scans	7
2.6 Schematic representation of scanning strategies commonly used in LSM (a) unidirectional long scan track; (b) bi-directional long scan track, and (c) islands	8
2.7 Samples (static tensile) built in different directions: (a) 0°, (b) 45°, and (c) 90°	8
3.1 ProX DMP 200 printer	11
3.2 Melt pool contours with and without laser compensation (exaggeration)	12
3.3 Laser compensations as a function of the scanning speed (as recommended by the manufacturer)	13
3.4 RODIA procedure for specimen X200-180319-cub 1: (a) Original picture of polished section (b) Whole surface isolation with <i>ImageJ</i> (c) Porosities isolation with <i>ImageJ</i>	15
3.5 Schematization of the Vickers hardness test	16
4.1 As-built apparent relative density and hardness results for samples of batch X200-171024 as a function of the energy density	18
4.2 As-built apparent relative density and hardness results of batch X200-180109 for (a) type "7" samples (b) type "8" samples.	19
4.3 Specimen X200-180417-25 sub-parts and surfaces denomination	20
4.4 RODIA based relative density and hardness results for specimen X200-180417-25 sample surfaces	21
5.1 50x magnification picture of specimen X200-180319-cub1 and delimitation of the zones A and B	24
5.2 Zone A of specimen X200-180319-cub1: (a) Delimitation from original picture under 50x magnification (b) Porosities isolation from 50x magnification picture (c) Original picture under 100x magnification (d) Porosities isolation of 100x magnification picture	26
5.3 Histograms of porosities areas occurrences from pictures of specimen X200-180319 on zone A under (a) 50x magnification (b) 100x magnification	27
A.1 Dimensions notations for (a) cubic specimens (b) cylindrical specimens	31

A.2 Specimens positions, order of fabrication and sintering times for batch X200-171024	32
A.3 Photography of the manufacturing plate after completion of the fabrication of batch X200-171024	32

List of Tables

2.1	Mechanical properties of SLM built parts and cast + aged parts in literature	9
3.1	Polishing routine for Al-Si alloys	14
3.2	Strain limits for interrupted tensile tests of batch X200-180417 specimens	16
4.1	Comparison of mean apparent relative densities and hardnesses of types 7 and 8 specimens of batch X200-171024	17
4.2	Composition of recycled AlSi10Mg powder as a function of the date	19
4.3	Tensile mechanical properties of the specimens from batch X200-180417	21
5.1	RODIA results for zones A and B of specimen X200-180317 with 50x and 100x magnification	25
A.1	Manufacturing process parameters	33
B.1	Extract of Vickers hardness conversion table (HV10)	35

List of Abbreviations

AB	As-Built
AM	Additive Manufacturing
CAD	Computer Aided Design
CI	Confidence Interval
DMLS	Direct Metal Laser Sintering
DMP	Direct Metal Printer
HPDC	High Pressure Die Casting
ICP	Inductively Coupled Plasma
RODIA	Relative Optical Density Image Analysis
SD	Standard Deviation
SEM	Scanning Electron Microscope
SLM	Selective Laser Melting

Symbols

D_a	Average particle size	$[\mu\text{m}]$
E	Young modulus	$[GPa]$
E_d	Volumetric energy density	$[\frac{\text{J}}{\text{mm}^3}]$
h	Hatch space	$[\mu\text{m}]$
H_v	Vickers hardness	$[HV]$
P	Laser power	$[W]$
p_{O_2}	Oxygen pressure	$[mbar]$
t	Layer thickness	$[\mu\text{m}]$
v_s	Scanning speed	$[\frac{\text{mm}}{\text{s}}]$
W_a	Specimen dry weight	$[g]$
W_w	Specimen underwater weight	$[g]$
ϵ_f	Strain at fracture	$[-]$
$\phi_{99\%}$	Laser spot size at the 99% contour	$[\mu\text{m}]$
λ	Laser wavelength	$[nm]$
ρ_a	Apparent density	$[\frac{\text{g}}{\text{cm}^3}]$
$\rho_{a,rel}$	Apparent relative density	$[-]$
ρ_w	Water density	$[\frac{\text{g}}{\text{cm}^3}]$
ρ_{rel}	Relative density	$[-]$
σ_u	Ultimate tensile strength	$[MPa]$
σ_y	Yield strength	$[MPa]$

Nous dédions ce travail à nos familles et amis

Chapter 1

Introduction

[This is, with the concluding chapter, a significant portion of memory. This should especially present the context and objectives of the work. Generally, the memory structure (content of chapters) is briefly exposed]

Chapter 2

State of the art

2.1 Selective laser melting technology

Selective laser melting (SLM) - also referred to as direct metal laser sintering (DMLS) - is an additive manufacturing (AM) technique making use of a high power-density laser that locally melts powder materials. When a layer of powder has been melted, a new layer is spread on top of the previous one, and is in turn melted, in order to progressively build a 3D object. The technique is illustrated on figure 2.1 [14]. The materials used include mostly metals but also ceramics and composites. Parts to build must first be drawn in a computer-aided design (CAD) software and broken down in 2D slices, each one corresponding to a powder layer. During the process, the oxygen pressure p_{O_2} must be kept low to prevent the oxidation of the metal. A shielding gas - such as argon - is thus used to fill the build chamber at all time, while p_{O_2} is monitored.

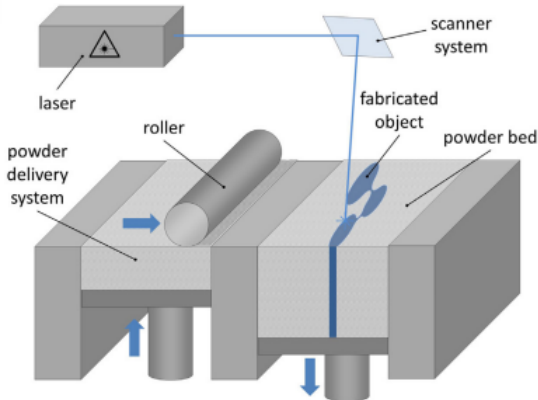


FIGURE 2.1: Selective laser melting technology principle (from Leitz et al., 2016).

LSM is still a young technology. Its popularity only increased significantly over the last decade, as depicted by figure 2.2). Works concerning AlSi10Mg began to emerge noticeably in 2014. The technique usage spread rapidly in many sectors: biomedical, heat exchangers, aerospace and automotive - to name just a few [28]. This is due to the numerous appeals of SLM compared to the other technologies, including:

- Geometrical flexibility: parts can be designed with thin walls or even with hidden cavities and/or channels. This offers promising prospects regarding light-weight potentials for parts solicited mechanically [16];
- Increased reliability of the parts [9];
- Reduced equipment costs [10];
- Better operational efficiency: the fabrication is quick and easy which reduces time-to-market as well as assembly times and capital tied up in stocks [10];
- Individual production facilitation [9];
- Reduced material waste and better energy usage: the process is environmentally friendly as a whole [9].



FIGURE 2.2: (a)Research publications on SLM of ceramics, composites and all materials types combined. (b)Research publications on SLM of different metallic materials. Data are derived from the research publications on SLM, LaserCusing and DMLS existing on ScienceDirect website.

The properties of parts produced through SLM stem from the coupled effects of a great deal of parameters (see figure 2.3) [3]. Results are very sensitive to their variations. The process parameters must thus be monitored thoroughly. This complicates the search for their optimisation, still not fully resolved for aluminium alloys.

In recent years, works aiming at facing this challenge multiplied. The minimisation of the porosity is at the center of attention. It is indeed closely related to the quality of the mechanical properties. As porosity contributes to lowering the load-bearing surface, it reduces the apparent material strength. It was also observed to have a critical influence on the fatigue life of the produced parts. Their lifetime is especially diminished if the values of pores amount and size go beyond a certain threshold [6]. Studies investigating the effects of various parameters on the AlSi10Mg fabrication through SLM abound in the literature.

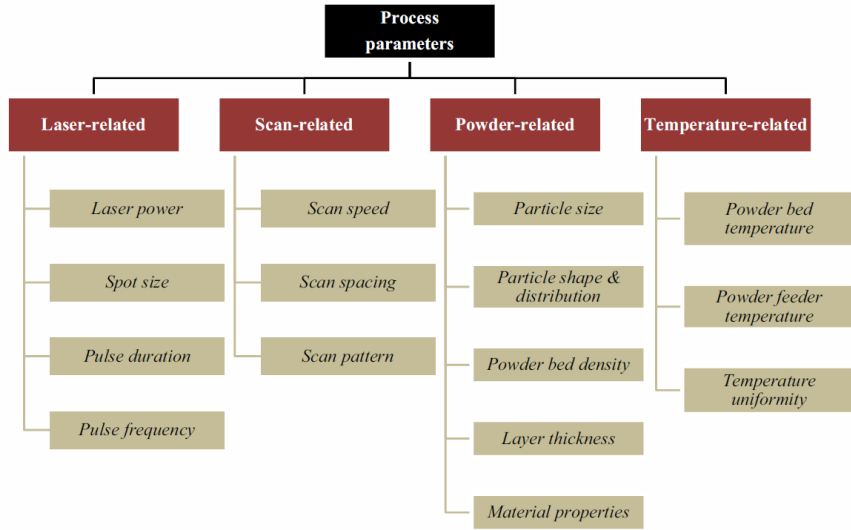


FIGURE 2.3: Parameters involved in SLM (from Aboulkhair et al., 2014).

2.2 AlSi10Mg alloy

Parler de l'AlSi10Mg; quel est l'intérêt de travailler avec? Difficultés? (reflectivité etc).. Qu'est ce qui existe en coulé, forgé etc
Microstructure homogène, diagramme de phase

Kempen dans "PROCESS OPTIMIZATION AND MICROSTRUCTURAL ANALYSIS FOR SELECTIVE LASER MELTING OF AlSi10Mg ":

AlSi10Mg is a typical casting alloy which is, due to its high strength/density ratio and thermal properties, highly demanded in aerospace and automotive industries [1]. The alloy combination of aluminium, silicon and magnesium results in a significant increase in strength and hardness which might even reach 300 MPa and 100 HBS, respectively, by applying a proper heat treatment [2]

Aluminium as a lightweight material is very attractive for the production of parts that require good mechanical properties in combination with a low weight. The main focus lies on Al-Si alloys, since they are casting alloys that are also suitable for welding. AlSi10Mg, which can be hardened by applying a specific heat treatment, is relatively easy to process by laser applications due to the small difference between liquidus and solidus temperature compared to high strength aluminium-alloys [2]. The AlSi10Mg alloy is frequently used in aerospace, automotive, chemical and food industry. Its composition according to ISO 3522 can be found in Table 1 [4]. Alloying the magnesium to the Al-Si alloy enables precipitation of Mg₂Si which will strengthen the matrix without compromising the other mechanical properties to a significant extent.

2.3 Fabrication process parameters

Let us now investigate the influence of the parameters on the properties of AlSi10Mg parts manufactured with SLM. The analysis of the paired impacts of the laser power P and scan speed v_s provides a first insight. As depicted by figures 2.4 and 2.5, low

P and high v_s lead to an insufficient energy input to melt the powder and re-melt the substrate, which causes the formation of droplets [13]. The opposite leads to good penetration but also to distortions and irregularities. A trend to use both high P and v_s rose in accordance with these findings. Doing so has the advantage to increase productivity. However, it also has multiple downsides including a decrease of the surface quality due to balling, excessive spatter, and an augmented gas induced porosity [18]. Therefore, a trade-off must be found.

A popular approach is to regroup multiple operating parameters into one, the volumetric energy density E_d . It is estimated through the following formula:

$$E_d = \frac{P}{v_s h t}$$

where t is the layer thickness and h is the hatch space. As a rule of thumb, E_d should be chosen in the range between 60 and 75 [$\frac{J}{mm^3}$] [21]. However, the criterion is insufficient and other phenomena, such as melt pools overlapping, should be considered [24]. Very few studies were carried out to optimize h and t independently. Their values lie generally in the intervals [50 ; 200] [μm] and [20 ; 60] [μm], respectively [2, 6, 13, 18]. It was observed that for $t = 30 [\mu m]$, an optimal set of parameters values in terms of density is $P = 200 [W]$, $v_s = 1400 [\frac{mm}{s}]$ and $h = 105 [\mu m]$ [13]. The apparent relative density $\rho_{a,rel}$ was then above 99.5 [%].

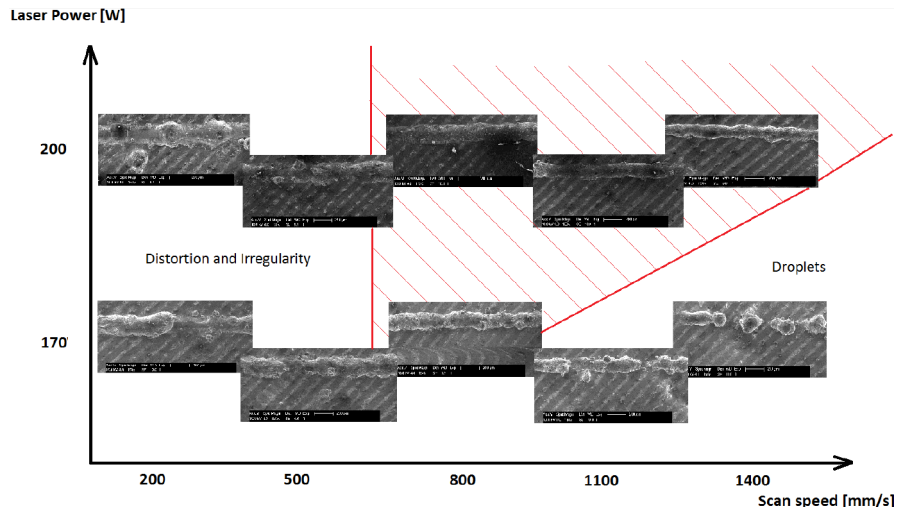


FIGURE 2.4: Process window for SLM of AlSi10Mg, based on the top view of single track scans (from Kempen et al., 2011).

The other process parameters will be covered for the sake of completeness. Let us first look into the particle-related parameters. The particle size D_a of the powder should be as small as possible to ensure a good flowability and allow for thin layers [13]. Typical values for mean particle size stretch from 15 to 50 [μm] but are more often at around 30 [μm] [6, 13, 19, 25]. The size distribution is more delicate to outline. On one hand, wider distributions often generate better bed density, parts with higher density and better surface finish. On the other hand, narrower ones usually provide better flowability and parts with better strength and hardness [17]. In most cases, a middle ground between the two should be sought. In SLM applications,

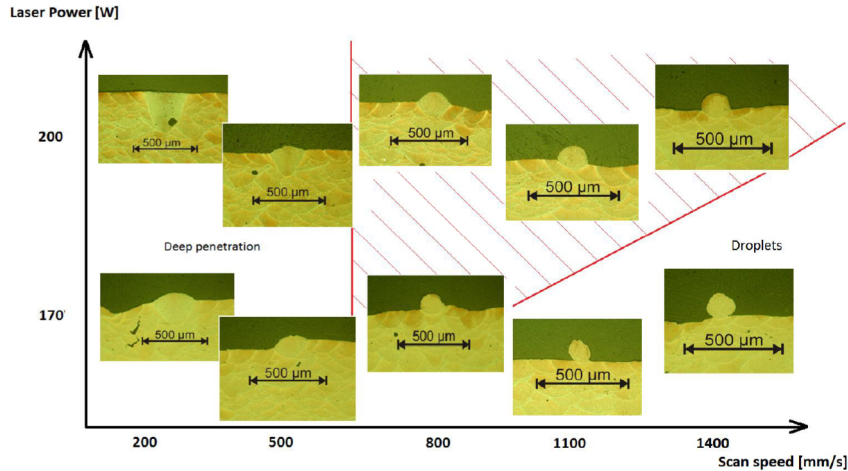


FIGURE 2.5: Process window for SLM of AlSi10Mg, based on the front view of single track scans (from Kempen et al., 2011).

powder is often successively recycled multiple times. This leads to their progressive contamination with moisture, which causes an increase of hydrogen porosity in the produced parts [27]. The problem can be overcome by drying the powder or using fresh one. Unfortunately - in the case of aluminium alloys - no findings were made regarding the prediction of a threshold at which one should take action [4].

The choice of scan pattern has great importance. There exist a few different strategies. The common ones use unidirectional, bidirectional or islands patterns (see figure 2.6). The scan direction(s) should always be rotated between successive layers to favorise isotropy, especially in the unidirectional case since it causes height variations along a layer [2]. The islands pattern is based on a decomposition in small domains with short scanning tracks. Two usual strategies can be distinguished among this group: the chessboard and the hexagonal one. A study proved the superiority of an island pattern over a bidirectional one in terms of both ultimate tensile stress σ_u and strain at fracture ϵ_f for a 316L stainless steel-Inconel 718 material [29]. It was also shown that it was possible to fabricate pure titanium samples without cracks using an island pattern, and not with a bidirectional one [15]. This is seemingly due to the greater accumulation of internal stresses and to the weaker interlayer bounding in the second case.

Furthermore, dual scanning strategies were proven to be effective. For example, a pre-scan with low E_d can flatten the powder bed before it is consolidated, which leads to a reduction of porosity [18]. It was also shown that scanning the contour of the part being built at lower E_d can better the surface roughness for AlSi12Mg [20]. One should note too that the final properties of the fabricated part can strongly depend on the building direction (see figure 2.7) [8]. Further properties comparison is provided in section 2.4.

Other laser-related parameters - the spot size and the pulse properties - can also influence the process. Only the laser spot size at the 99% contour $\phi_{99\%}$ is frequently cited in literature. Its value lies between 20 and 200 μm [6, 13, 19]. At this moment, no optimisation study was carried out about this variable. One should expect the optimal value for P , v_s , t , and h to depend on the spot size as it has a direct incidence

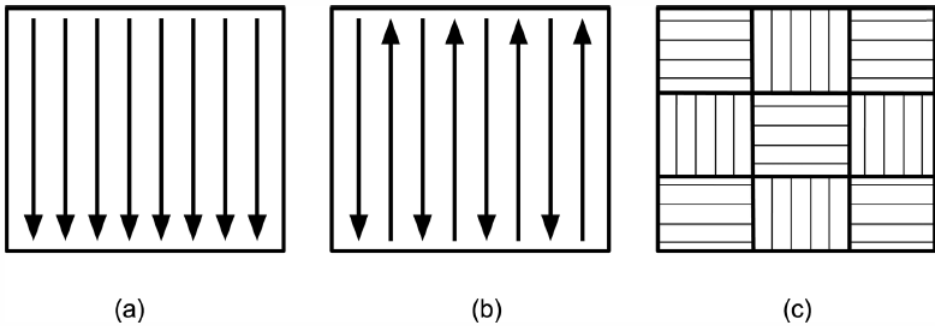


FIGURE 2.6: Schematic representation of scanning strategies commonly used in LSM (a) unidirectional long scan track; (b) bi-directional long scan track, and (c) islands (from Mertens et al., 2017).

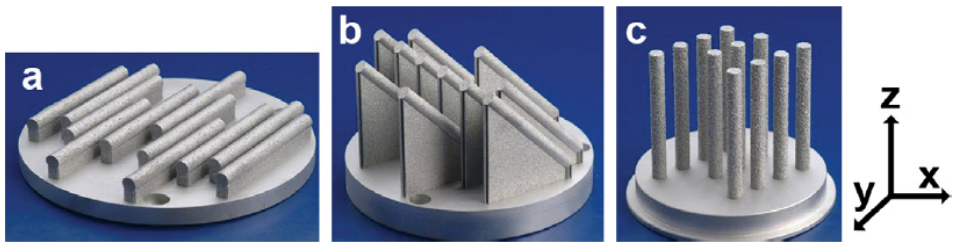


FIGURE 2.7: Samples (static tensile) built in different directions: (a) 0° , (b) 45° , and (c) 90° (from Brandl et al., 2012).

on E_d .

Finally, the temperature of the powder bed and feeder affect the final properties of the fabricated parts as well. In particular, it was observed that pre-heating the powder at 300° C mitigates the differences of fatigue resistance between tensile specimens built in different directions: it is possible that the operation induces a slower cooling rate which helps reducing the distortions and internal stresses [6].

Once the porosity problem is sorted out, other matters can be addressed such as productivity and surface roughness. The latter is problematic as the surface finish obtained with SLM is typically of such poor quality that all cracks initiate near the surface for a sample with relative density $\rho_{rel} > 99\%$ [6]. As said before, it is possible to reduce the surface roughness by mean of a dual scan strategy. However, the only options to obtain significantly better surface finish is currently to machine or polish the fabricated parts. This is one of the main weak points of SLM.

2.4 As-built mechanical properties

In a work of Kempen et al., as-built (AB) additively manufactured AlSi10Mg samples were observed to have mechanical properties (Vickers hardness HV , ultimate tensile stress σ_u , fracture strain ϵ_f and impact energy) better or at least comparable to the conventionally casted and high pressure die casted (HPDC) alloy [12]. The tensile

specimens built in an horizontal direction (XY) had slightly different characteristics than those built in the vertical direction (Z). The results obtained in the mentioned work are gathered in table 2.1, along with other results with $\rho_{rel} > 99.94[\%]$ and common cast AlSi10Mg properties.

Process	Young Modulus [GPa]	σ_u [MPa]	ϵ_f [%]	HV [HV]
SLM - XY direction [12]	68 ± 3	391 ± 6	5.55 ± 0.4	127
SLM - Z direction [12]		396 ± 8	3.47 ± 0.6	
SLM [5]	77 ± 5	333 ± 15	1.4 ± 0.3	125 ± 1
SLM - XY direction [19]	65.5	358	3.9	-
SLM - Z direction [19]	75.4	289	2.6	-
Conventional cast and aged [12]	71	300-317	2.5-3.5	86
As built HPDC [12]		300-350	3-5	95-105
T6 treated HPDC [12]		330-365		130-133

TABLE 2.1: Mechanical properties of SLM built parts and cast + aged parts in literature

2.5 Post treatments

Post-traitements dont traitements thermiques, sur lesquels on se focalise. Expliquer Source que tu peux utiliser:

Trevisan et al, 'On the Selective Laser Melting (SLM) of the AlSi10Mg Alloy: Process, Microstructure, and Mechanical Properties' (AlSi10Mg de manière générale)

Anne Mertens: 250 deg/2h <https://orbi.uliege.be/bitstream/2268/185421/1/2015-SFFS-Mertens.pdf>

Traitement T6 [5]

<http://sci-hub.tw/> <https://www.sciencedirect.com/science/article/pii/S0921509316304890>

Chapter 3

Materials and methods

3.1 Powder follow-up

3.1.1 Sieving

3.1.2 Grain size and distribution

3.1.3 Composition

3.2 Manufacturing parameters

The same direct metal printer (DMP) was used to fabricate all specimens throughout this work. It is a *ProX DMP 200* printer, manufactured by *3D Systems* (see figure 3.1). It uses a laser with a theoretical maximal power of 300 [W] and wavelength $\lambda = 1070$ [nm] [1]. Its actual maximal power is $P_{max} = 273.6$ [W]. [QUEL EST LE SPOT SIZE?] The maximal envelope capacity of the machine (W x D x H) is 140 x 140 x 125 [mm]. Its typical accuracy is +/- 50 [μm] for small parts and +/- 0.2% for large parts. It allows for the set-up of a protection atmosphere. However, it does not integrate any heating feature for the build bed.



FIGURE 3.1: ProX DMP 200 printer (from the user's ProX DMP 200 general instructions document).

In this thesis, argon was used as shielding gas. The composition of the gas environment was monitored so as to keep $p_{O_2} < 500$ [ppm]. Laser compensations were set to take into account the excess energy at the start and end of the scanning vectors (see figure 3.2). These were chosen in accordance with the manufacturer recommendations (figure 3.3). Values for h and t were respectively set to 100 [μm] and 30 [μm]. The other process parameters were varied so as to optimize the properties of the built specimens. Educated guesses were made based on literature and previous works done at the UCL. The parameters used are resumed in appendix A.1. Batches were named in the format X200-yyymmdd. The prefix "X200" refers to the DMP used. It is followed by the date of printing (6 digits). Recycled powder was used for every batch except for X200-180222 and X200-180228. In the case of samples with contour scanning strategy, the contours were pre scanned for each powder layer with the same P and v_s used for the bulk.

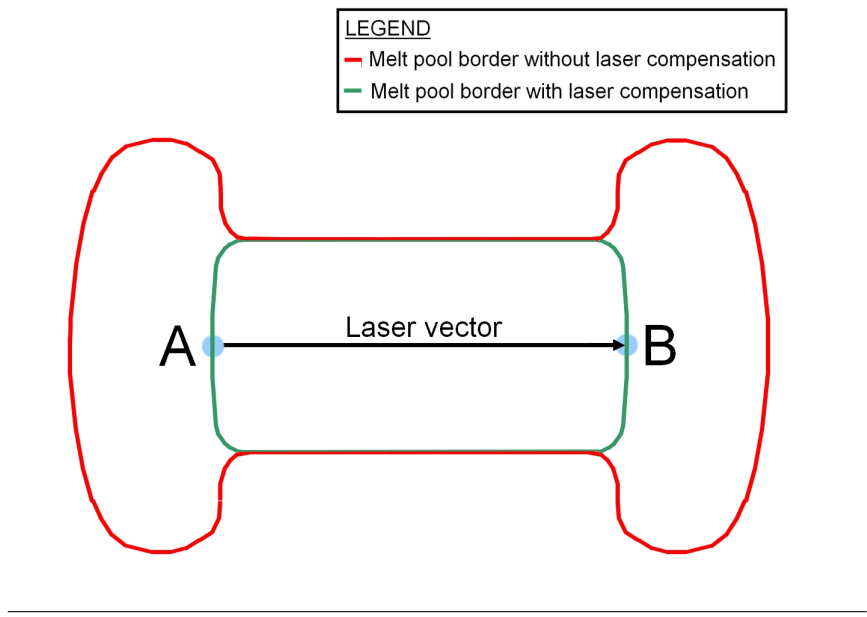


FIGURE 3.2: Melt pool contours with and without laser compensation (exaggeration).

All batches were first prepared on *DMP ProX Manufacturing*, a dedicated CAD software. It enabled to select the values for the parameters previously mentioned, as well as the position of the specimens. For this thesis, all cylinders and tensile specimens were fabricated vertically. [Parler des éprouvettes utilisées, dimensions? -> Dessin]

An island scanning strategy was chosen on account of research done on the subject (see section 2.3). It is a hexagonal pattern with [OVERLAP? TAILLE DES HEXAGONES?] The scanning order was automatically chosen. Figures with detailed specimens positions, denominations, scanning orders and sintering durations are available in appendix A.2.

[Insérer images de trajets du laser].

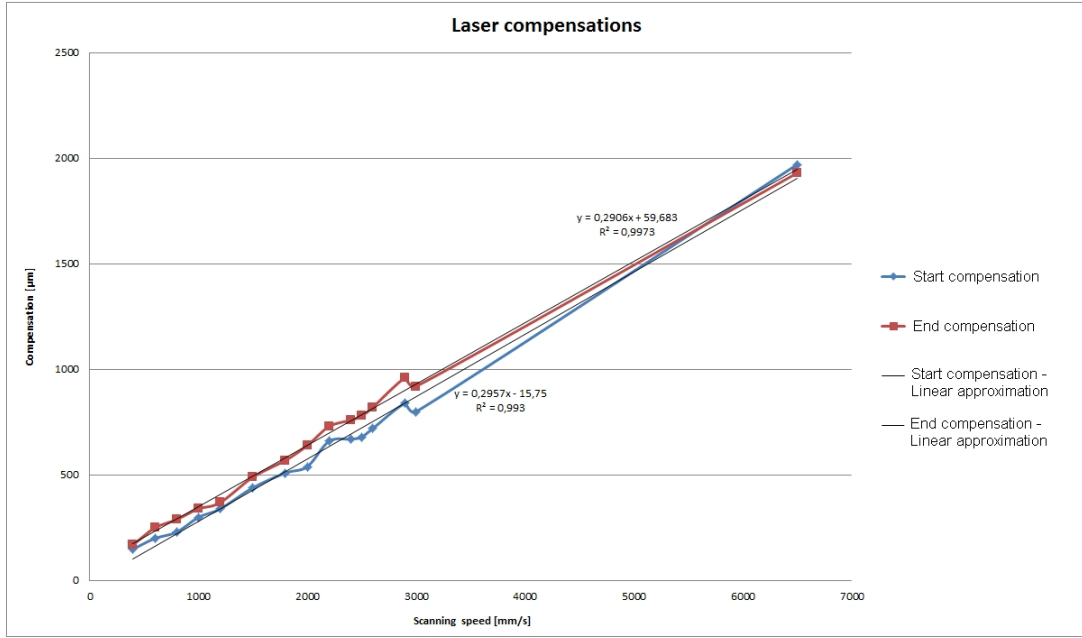


FIGURE 3.3: Laser compensations as a function of the scanning speed (as recommended by the manufacturer).

3.3 Heat treatments

The heat treatments were conducted inside a unique oven of the VT 5050 EKP model, manufactured by Heraeus, which is able to reach a temperature of 400° C. Samples temperature data was obtained through a thermocouple welded to the sample surface. [Méthode de soudage, élévation de la température durant l'opération] The data was displayed and saved every 10 seconds, with a precision of 0.1° C, thanks to a Agilent 34972A LXI Data Acquisition/Switching Unit, connected to the thermocouple (see Fig. for both devices).

Samples that were subject to a heat treatment were named in a particular format, to ease distinction between them. They received the name of the batch, followed by "TT-holdingtemperature-holdingtime-specificities".

3.4 Characterisation

3.4.1 Density

Hydrostatic weighing

Multiple methods were considered to estimate the relative density of the fabricated specimens. The first one is hydrostatic weighting (also called hydrodensitometry). It is a direct application of the well-known Archimedes' principle, which can be stated as follows: " When a body is (partially or totally) immersed in a fluid, the upthrust on the body is equal to the weight of fluid displaced." [7]. By weighing each pieces in air and in water - giving respectively values of dry weight W_a and underwater weight W_w - one can calculate the apparent density ρ_a [11]:

$$\rho_a = \frac{W_a}{W_a - W_w} \cdot \rho_w$$

where ρ_w is the water density. The apparent relative density $\rho_{a,rel}$ of the specimens can then be calculated with:

$$\rho_{a,rel} = \frac{\rho_a}{\rho_b}$$

where $\rho_b = 2.68[\frac{g}{mm^3}]$ is the theoretical bulk density of AlSi10Mg [22]. All weightings were done with a *Sartorius BP121S* analytical balance with precision of 0.1 [mg] [23]. Samples were immersed in demineralised water for more than twelve hours before the measurements to impregnate them. The weightings were also done in demineralised water. Water temperature was measured with a precision glass thermometer to compute ρ_w as accurately as possible thanks to tabulated values [26]. Multiple measurements were done for each sample in order to increase the method's reliability.

The technique was employed with "as-built" and polished cubes. For this second option, all six faces of the tested cubes were polished with P320 silicon carbide sandpaper sheets and briefly with P1200 ones.

Relative optical density image analysis

Another method was used to estimate the relative density of the various samples: the relative optical density image analysis (RODIA). For this purpose, the samples were cut with a micro-cutting machine and underwent the polishing routine detailed in table 4.3. Pictures of the polished sections were then taken under the optical microscope. An *Olympus AX70* microscope was used, with 5x and 10x magnification. The pictures were taken with a smart-phone through the lens of the microscope. The used camera has a resolution of 16 [MP]. A camera is directly connected to the microscope at the laboratory, but it only has 5 [MP] resolution. It was thus chosen not to use it.

With the help of the *ImageJ* software, the surface of both the porosities and the whole surface could be isolated for each analysed image (see figure 3.4). The surface fraction occupied by porosities could then be obtained as the ratio between the areas of the two (in pixels). If we approximate that the porosities surface fraction is equal to the volumetric one, that method gives an estimation of the relative density ρ_{rel} .

Step	Polishing surface	Abrasive	Grain size	Lubricant type	Rotation speed [rpm]
1	MD-piano 220	Diamond	P220	Water	200-300
2	MD-piano 1200	Diamond	P1200	Water	200-300
3	MD-largo	DP-spray	9 μm	Alcohol	150
4	DP-DAC	DP-spray	3 μm	Alcohol	150
5	DP-NAP	DP-spray	1 μm	Alcohol	150

TABLE 3.1: Polishing routine for Al-Si alloys

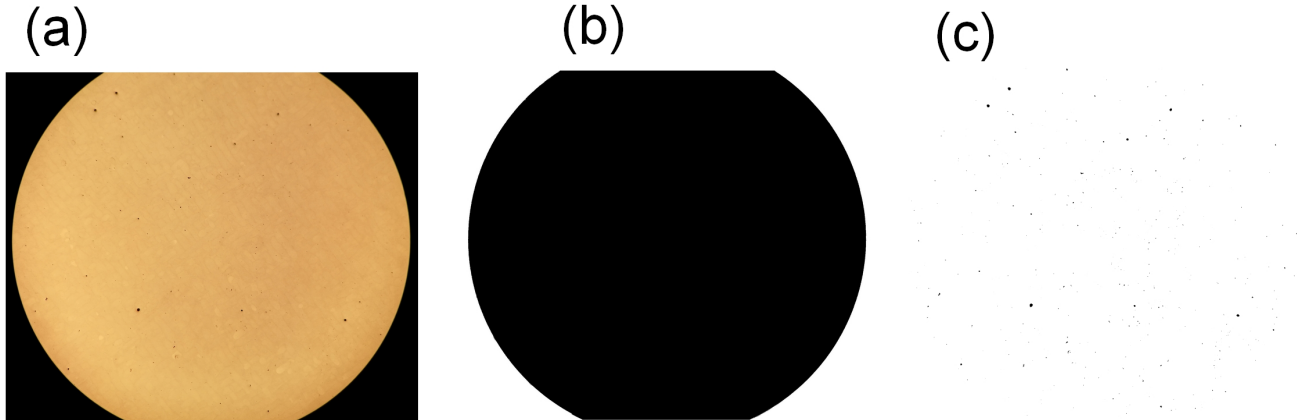


FIGURE 3.4: RODIA procedure for specimen X200-180319-cub 1: (a) Original picture of polished section (b) Whole surface isolation with *ImageJ* (c) Porosities isolation with *ImageJ*.

The images isolations in "foregrounds" and "backgrounds" were done through manual thresholding based on pixel intensity quantifications. An optimal threshold was sought for porosities isolation so as to include only holes, and as many as possible. Particular attention was given to the photography in order to obtain the best contrast, focus and intensity homogeneity. Several pictures were taken for each specimen to build a representative sample.

3.4.2 Microstructure

Scanning electron microscopy

Optical microscopy

Mesures Taille de bains Densité Autre chose?

3.4.3 Composition

3.4.4 Internal stress

3.4.5 Mechanical properties

Hardness test

Vickers hardness measurements were made with a *Wolpert Dia-Testor 2RC* tester. All analysed specimens were previously cut with a micro-cutting machine to enable the measurement of the bulk hardnesses of the samples (at least at a few millimetres from the initial surfaces). For each test, a pyramidal indenter (see figure 3.5) was pressed during 10 [sec] onto the material with a load of 10 [kg]. The indentation durations were measured with a digital timer and the tests were stopped manually. The two diagonals lengths of the resulting indents were then evaluated using a ruler on the screen of the machine, which displays the image of the sample's surface that is captured by an embedded optical microscope.

Multiple tests were made for each sample and the mean diagonal length value was computed for every test. The corresponding Vickers hardness values HV could

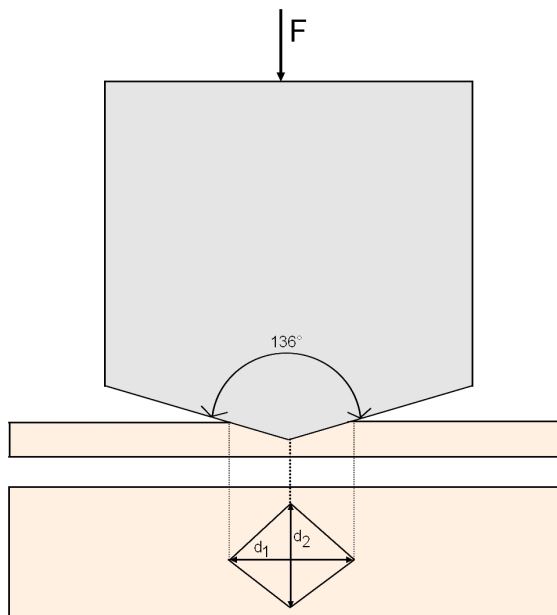


FIGURE 3.5: Schematization of the Vickers hardness test

then be estimated by means of a conversion table.

Tensile tests

The traction tests were performed on [Machine?]. The tensile specimens used all originated from batch X200-190417. Details about their geometry and heat treatments can be consulted respectively in sections 3.2 and 3.3. [Fonctionnement de la machine] [Calcul des caractéristique matériau]

For each test, the extensometer gauge length was set to 18 [mm] and the pre load to 15 [N]. A cross head speed of 1 [$\frac{mm}{min}$] was chosen. It was decided to interrupt the tensile tests of one specimen of every group that underwent the same heat treatment. In that way, the damage mechanisms could be observed afterwards. Table 3.2 regroups the strain limits at which the tests were stopped.

Sample	Strain limit [-]
X200-180417-3	0.01
X200-180417-6	0.06
X200-180417-9	0.08

TABLE 3.2: Strain limits for interrupted tensile tests of batch X200-180417 specimens

Chapter 4

Results

4.1 Parameters optimisation

The optimisation of the manufactured samples properties was done with respect to $\rho_{a,rel}$ and H_v by means of P and v_s variation. For this purpose, twelve cubes were fabricated in batch X200-171024. Details about the batch are given in appendix A. The goal of this optimisation was to select a single set of parameters values to use in the rest of the thesis. The parameters values were chosen to cover a wide range of E_d . Sets of values of types "7" and "8" are the ones that gave the best results in terms $\rho_{a,rel}$ in a previous work done at UCL. It was decided to produce samples with the corresponding P and v_s in triplicate in order to have a first insight on the process reproducibility.

Results for the measurements of $\rho_{a,rel}$ and H_v are displayed in figure 4.2. The 95% confidence intervals (CI) are also drawn. The methods used to compute them are described in appendix C. All apparent relative density values were obtained through hydrostatic weighing of the unpolished AB specimens.

The graph shows a general progressive decrease of $\rho_{a,rel}$ and H_v for $E_d > 57[\frac{J}{mm^3}]$. The samples of type "7" have both best $\rho_{a,rel}$ and H_v in average. The standard deviations (SD) of the values are also significantly better than the one of type "8" (see table 4.1). One should note that density and hardness values were respectively rounded with four and three significant figures in accordance with the CI sizes. Sample 4 exhibited good properties, comparable to the type "7" specimens. Surprisingly, the worst $\rho_{a,rel}$ measured is that of sample 8a with a value of 98.77[%].

Type	$\rho_{a,rel}$ [%]	$SD_{\rho_{a,rel}}$ [%]	H_v [HV]	SD_{H_v} [HV]
7	99.42	0.08	138	0.4
8	99.08	0.27	135	1.3

TABLE 4.1: Comparison of mean apparent relative densities and hardnesses of types 7 and 8 specimens of batch X200-171024

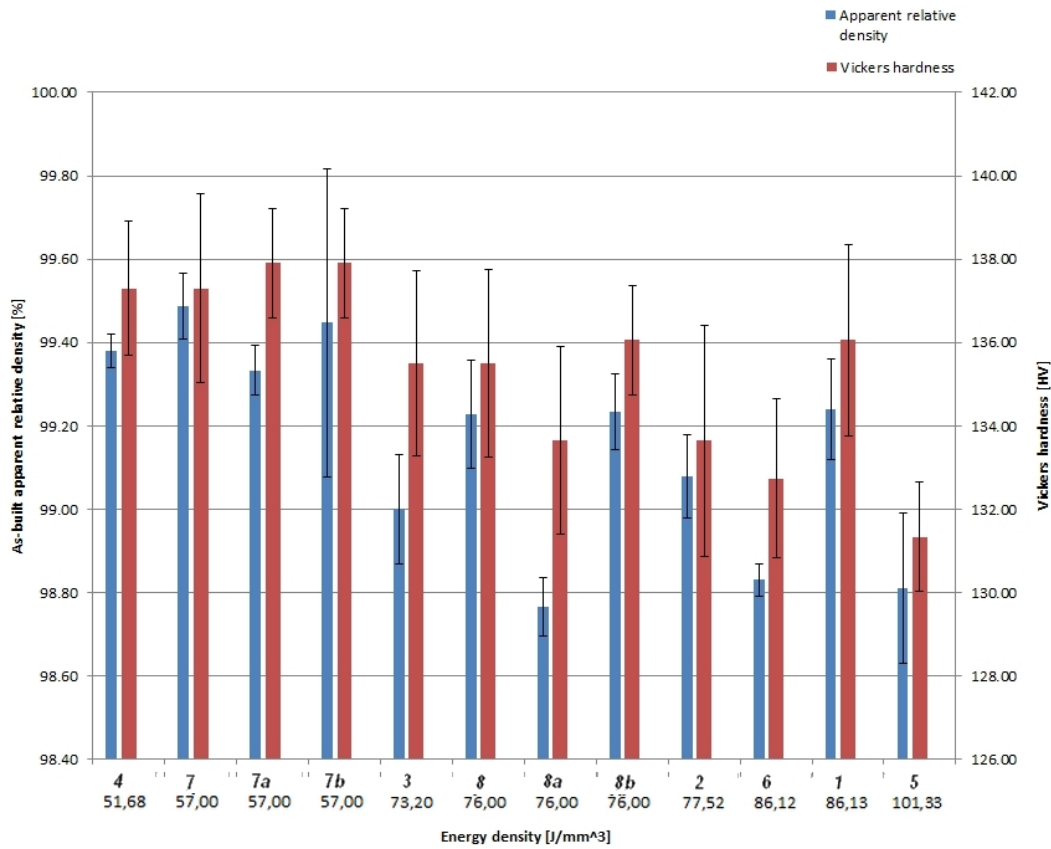


FIGURE 4.1: As-built apparent relative density and hardness results for samples of batch X200-171024 as a function of the energy density

4.2 Reproducibility

4.2.1 Relative density and hardness

Generalities

Position influence

Proximity influence

Time influence

4.2.2 Melt pool size and distribution

4.3 Internal properties homogeneity

As said in section 3.2, all tensile specimens were fabricated vertically. Their height is significantly greater than the other samples'; respectively 6 [cm] and 1 [cm] or less. It was chosen to cut up specimen X200-180417-25 into slices to measure if the density and hardness were homogeneous along the Z direction in the material. The surfaces analysed were named according to their original Z position in the specimen with "B", "C1", "C2", "C3" and "T" (for bottom, center and top) and to the test done with a letter "D" or "H" (for density and hardness). The denomination is summarised in figure 4.3.

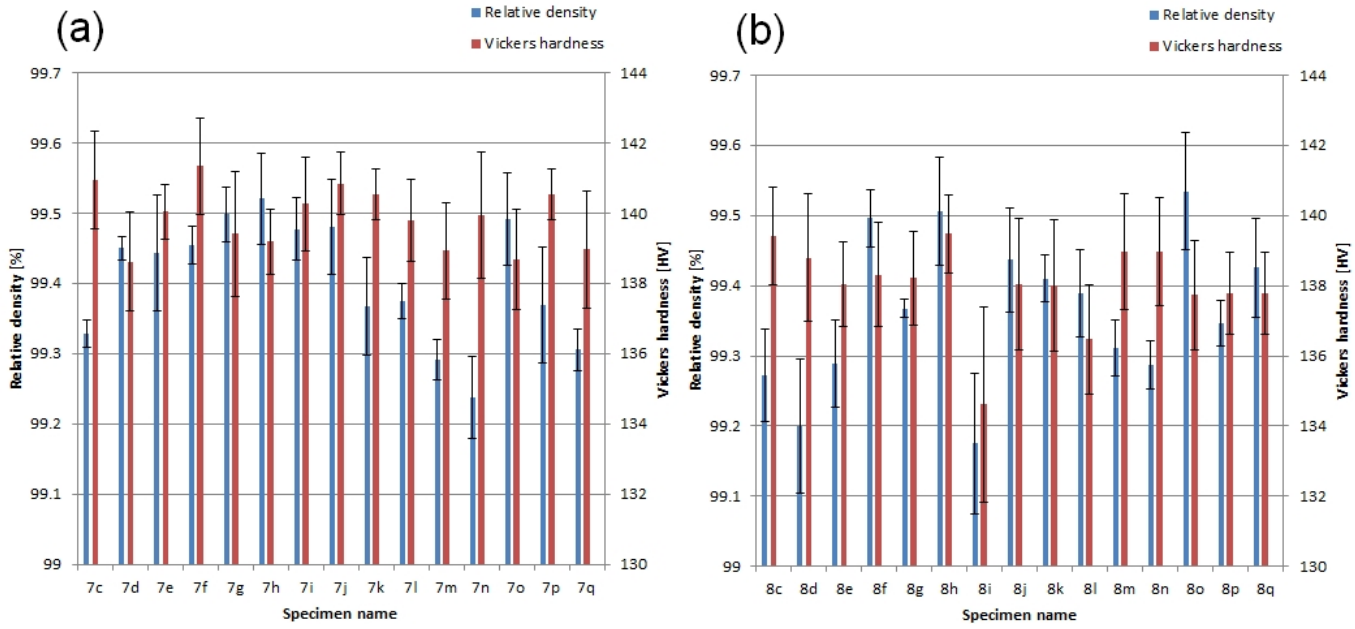


FIGURE 4.2: As-built apparent relative density and hardness results of batch X200-180109 for (a) type "7" samples (b) type "8" samples.

Results are shown on figure 4.4.

4.4 Powder ageing

4.4.1 Grain size and distribution

Fresh powder

Recycled powder

4.4.2 Composition

Fresh powder

Recycled powder

Date of sampling	Date of last addition of fresh powder	Composition [%wt]			
		Al	Fe	Mg	Si
23/10/2017	07/09/2017	89.2	0.12	0.49	10.2
09/01/2018	07/09/2017	89.3	0.13	0.48	10.1
12/01/2018	07/09/2017	89.4	0.13	0.48	10
21/02/2018	07/09/2017	89.1	0.19	0.51	10.3
13/03/2018	22/02/2018	89.1	0.16	0.51	10.1

TABLE 4.2: Composition of recycled AlSi10Mg powder as a function of the date

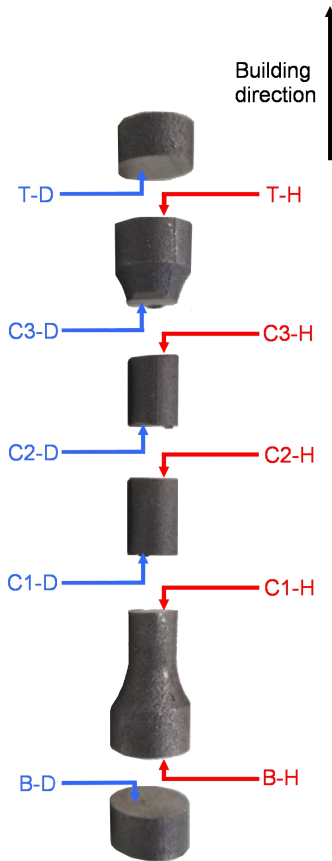


FIGURE 4.3: Specimen X200-180417-25 sub-parts and surfaces denomination.

4.5 Heat treatments

4.5.1 Heating process

The main objective of most of the research about aluminium alloys AM is to obtain parts with properties at least as good as their conventional cast counterparts. To obtain a larger panel of properties, a vast number of heat treatments have been developed for die cast alloys.

4.5.2 Microscopy

4.5.3 Hardness testing

4.5.4 Tensile testing

4.5.5 Internal stress testing

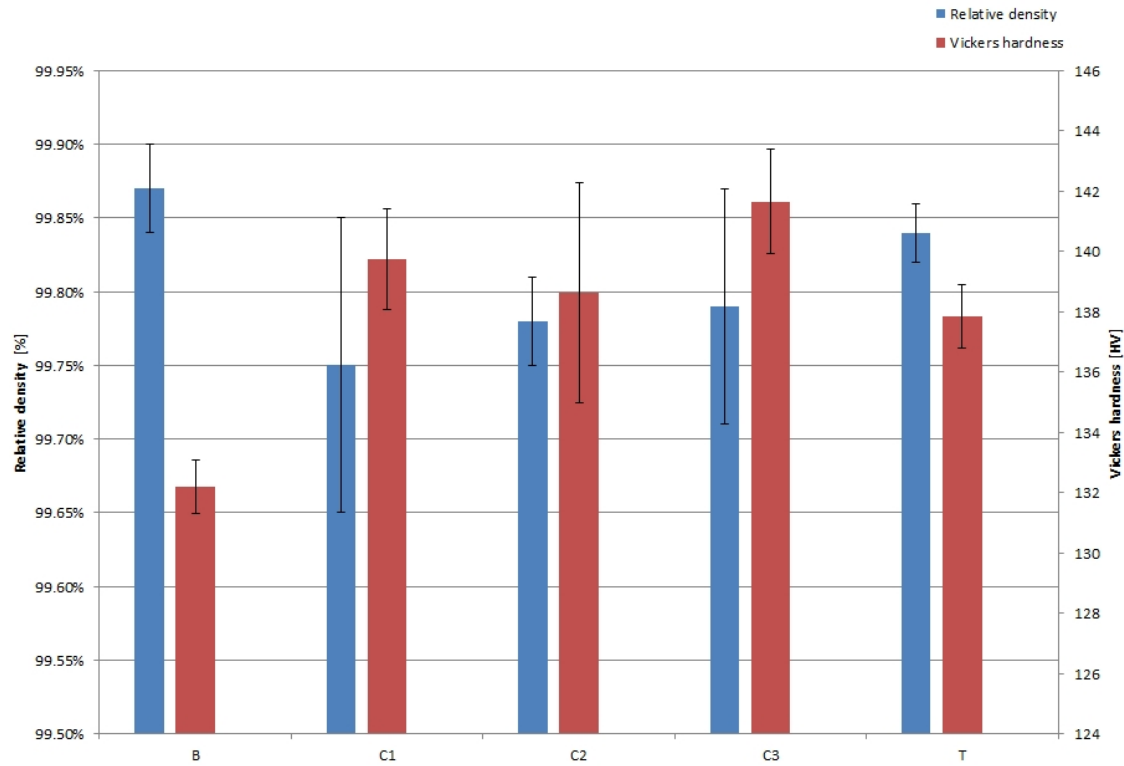


FIGURE 4.4: RODIA based relative density and hardness results for specimen X200-180417-25 sample surfaces

Specimen	Contour	TT	E [GPa]	σ_y [MPa]	σ_u [MPa]	ϵ_f [%]
X200-180417-1	Yes	None	74.6	260.8	366.4	2.2
X200-180417-2	Yes	None	68.2	290.2	388.3	2.4
X200-180417-3	Yes	None	64.0	275.9	-	-
X200-180417-A	No	None	61.0	257.1	379.2	2.8
X200-180417-13	Yes	150°C (2h)				
X200-180417-14	Yes	150°C (2h)				
X200-180417-15	Yes	150°C (2h)				
X200-180417-B	Yes	150°C (2h)				
X200-180417-10	Yes	200°C (2h)				
X200-180417-11	Yes	200°C (2h)				
X200-180417-12	Yes	200°C (2h)				
X200-180417-7	Yes	250°C (2h)	72.2	230.7	334.5	9.1
X200-180417-8	Yes	250°C (2h)	70.2	238.9	347.4	8.6
X200-180417-9	Yes	250°C (2h)	71.3	227.7	$\simeq 328.7$	-
X200-180417-4	Yes	300°C (2h)	81.6	164.4	249.6	14.1
X200-180417-5	Yes	300°C (2h)	68.4	172.4	256.24	13.1
X200-180417-6	Yes	300°C (2h)	68.6	168.5	$\simeq 242.5$	-

TABLE 4.3: Tensile mechanical properties of the specimens from batch X200-180417

Chapter 5

Discussion

Que conclure d'après les résultats?

5.1 Parameters optimisation

5.2 Reproducibility

5.2.1 Melt pool size distribution

5.3 Powder ageing

5.3.1 Grain size and distribution

5.3.2 Composition

5.4 Density measures assessments

5.4.1 Hydrostatic weighing

This second option reduces the risks of air trapping by the surface roughness, which can distort the results (by overestimating the closed porosities volume).

5.4.2 Relative optical density image analysis

The estimation of the relative density through RODIA can be distorted on many grounds. First, the distribution of porosities is inhomogeneous on the analysed surface. Multiple photos must thus be taken with a systematic manner for each specimen to constitute a representative sample.

Second, the quality of the photographs has a critical role. The isolation of the porosities during the thresholding requires a substantial difference of pixel intensity between the holes and the material. Since some porosities and some zones of the material can appear respectively brighter or darker than what is expected, there are risks that one isolates spots and/or not actual porosities. Additionally, the thresholding is manual and thus prone to slight human errors.

Most importantly, the finite resolution of the camera implies that sufficiently small porosities are not visible on the pictures. The exact shape of the holes are also imperfectly transcribed due to the discretization in pixels. Results for pictures with different magnifications were compared to quantify these effects. For this purpose, a picture was taken under 5x magnification and two under 10x magnification. The former was delimited to match the visible zones on the latter (see figure 5.1).

The same two zones - named A and B - were thus analysed for different levels of resolution.

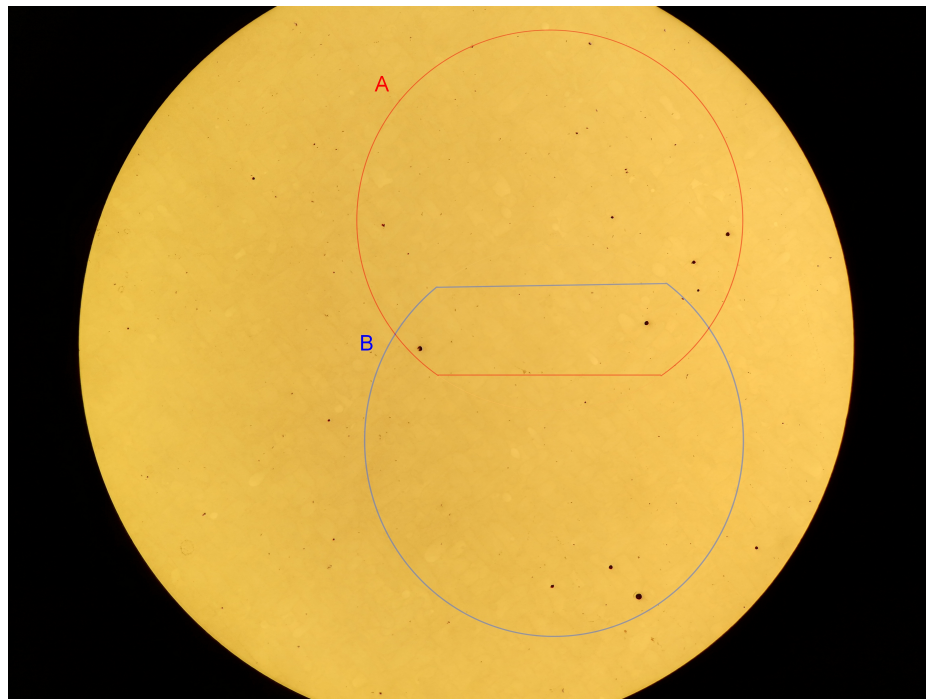


FIGURE 5.1: 50x magnification picture of specimen X200-180319-cub1
and delimitation of the zones A and B

The comparison of figures 5.2 (b) and (d) shows that much more small porosities are isolated if the resolution is refined - as expected. This is confirmed by the histograms on figure 5.3. The threshold of porosity area for detection in the case of 5x magnification is $7.84 \text{ } [\mu\text{m}^2]$ whereas it is $1.96 \text{ } [\mu\text{m}^2]$ for 10x magnification. This area corresponds to a pixel in each case. It is also worth noting that there is an overall tendency to overestimate the areas at lower resolution, which counterbalances slightly the low number of detected porosities.

The RODIA results for zones A and B are outlined in table 5.1. The lack of resolution seems to cause an overestimation of a few hundredths of percent of the relative density. The method is thus presumably positively biased. However, the observed effect is minor: this is probably due to the fact that the undetected porosities are the smallest, which influence the less the calculated density value.

Taking pictures at refined magnification could be considered to better the precision of the method. This would, however, require to augment the number of analysed pictures to have a sample of pictures as representative. A picture with doubled magnification covers indeed four times less surface. The number of analysis should thus be quadrupled to take as much information into account.

Zone	Magnification	Measured relative density [%]
A	50x	99.87
A	100x	99.84
B	50x	99.86
B	100x	99.85

TABLE 5.1: RODIA results for zones A and B of specimen X200-180317 with 50x and 100x magnification

5.5 Measures comparison

5.6 Heat treatments

5.6.1 Heating process??

5.6.2 Microstructure

5.6.3 Mechanical properties

5.6.4 Internal stress

5.6.5 Optimisation

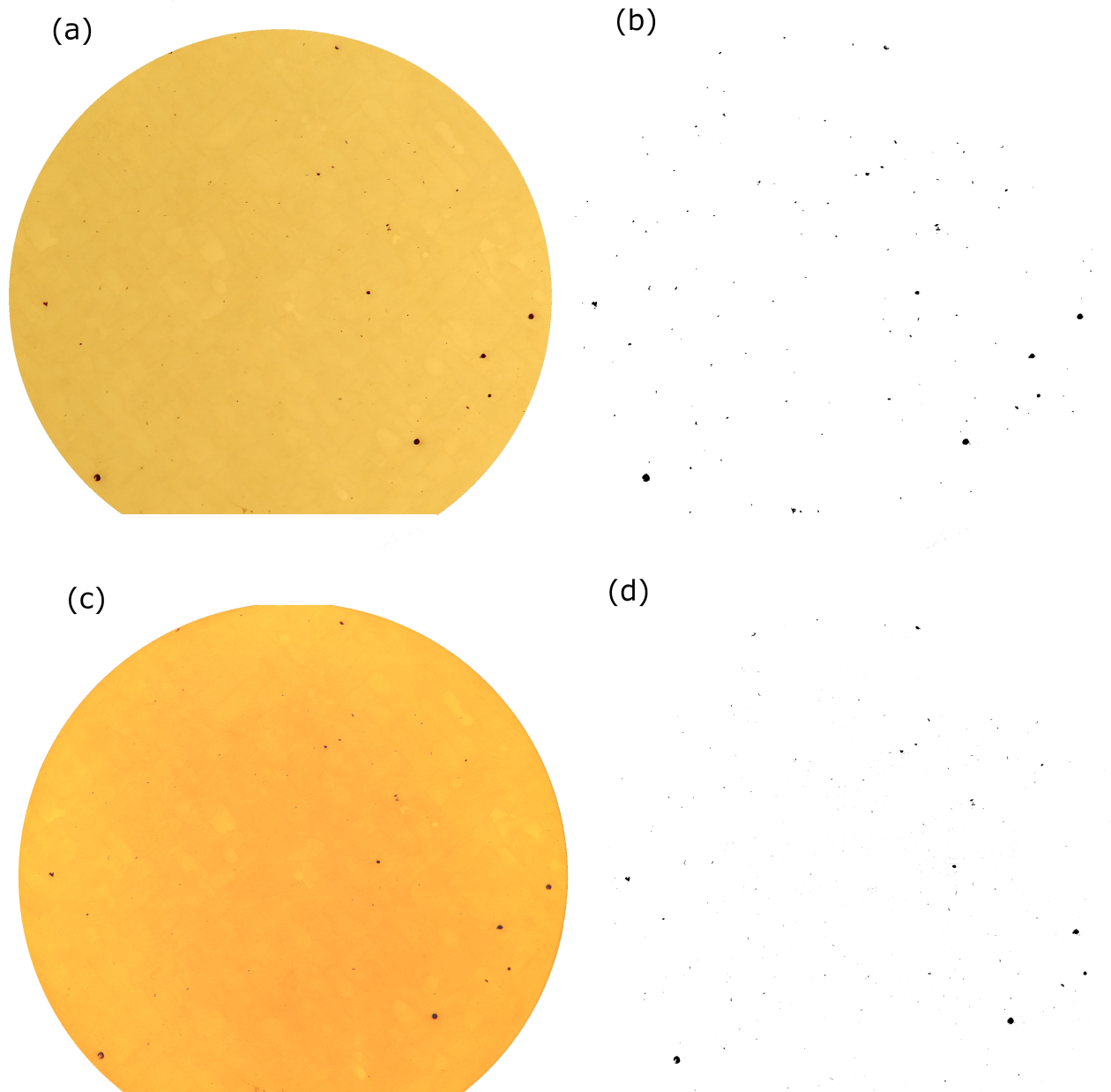


FIGURE 5.2: Zone A of specimen X200-180319-cub1: (a) Delimitation from original picture under 50x magnification (b) Porosities isolation from 50x magnification picture (c) Original picture under 100x magnification (d) Porosities isolation of 100x magnification picture

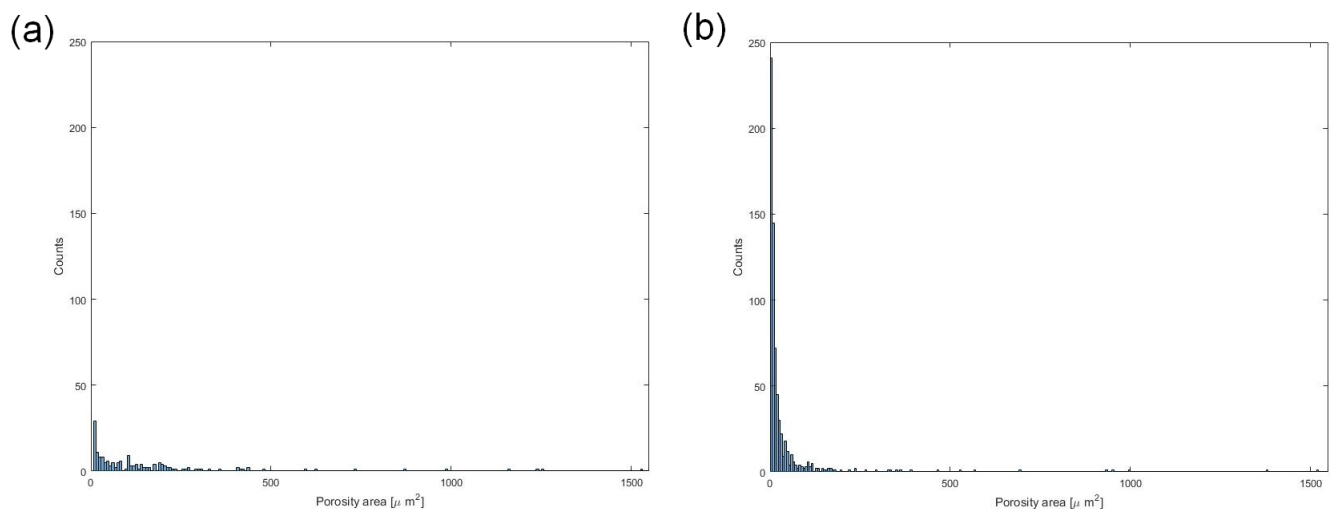


FIGURE 5.3: Histograms of porosities areas occurrences from pictures of specimen X200-180319 on zone A under (a) 50x magnification (b) 100x magnification. Truncation along the x axis.

Chapter 6

Conclusion

They incorporate in a synthetic way the main results and compare them with the initial objectives. Generally, this final chapter also presents prospects for the continuation of the work undertaken.

Appendix A

Batches fabrication details

A.1 Process parameters

Dimensions of the cubic and cylindrical specimens are noted in accordance with figure A.1. [AJOUTER DERNIER BATCH]

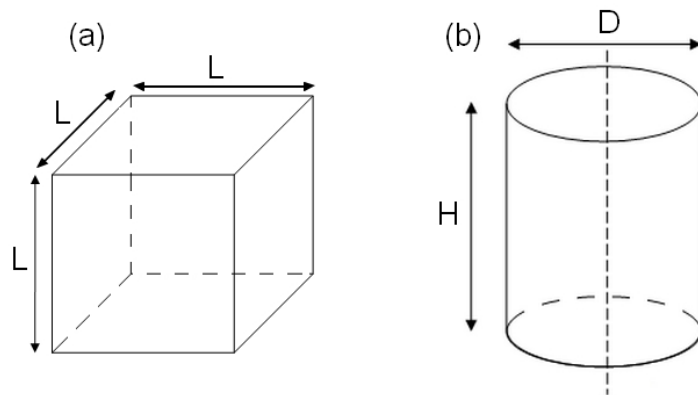


FIGURE A.1: Dimensions notations for (a) cubic specimens (b) cylindrical specimens

A.2 Specimens positioning, fabrication orders and sintering times

A.2.1 Batch X200-171024

A.2.2 Batch X200-180109

...

A.2.3 ...Other batches



FIGURE A.2: Specimens positions, order of fabrication and sintering times for batch X200-171024



FIGURE A.3: Photography of the manufacturing plate after completion of the fabrication of batch X200-171024

Batch name	Contour	Type	Dimensions [mm]	Specimen name	$\frac{P}{P_{max}} [-]$	$v_s [\frac{mm}{s}]$
X200-171024	No	Cubic	L=10	1 2 3 4 5 6 7, 7a, 7b 8, 8a, 8b	0.85 1 0.75	900 1000 1059 1500 900 1059 1200 900
X200-180109	No	Cubic	L=10	7c,...7q (15 spec.) 8c,...8q (15 spec.)	0.75	1200 900
X200-180220	No	Cubic	L=5	TT150-2 TT200-2 TT300-2 TT300-2-plaque TT150-2-real TT200-2-real TT250-2-real TT300-2-real	0.75	1200
X200-180222	No	Cubic	L=10	12 13	0.75	1200
X200-180228	Yes	Cylindrical	D=6, H=2	1 2 3	0.75	1200
X200180313	Yes	Cylindrical	D=6, H=10 D=12, H=10	1 2 3 4	0.75	1200
X200-180319	No	Cubic	L=10	cub 1 cub 2 cub 3 cub 4 cub 5	0.75	1200
	Yes	Cylindrical	L=5 D=6, H=10 D=12, H=10	TT300-1-real cyl 1 cyl 2 cyl 3 cyl 4		

TABLE A.1: Manufacturing process parameters

Appendix B

Extract of Vickers hardness conversion table (HV10)

Diagonal length [mm]	0	1	2	3	4	5	6	7	8	9
0.34	160	160	159	158	157	156	155	154	153	152
0.35	151.4	150.5	149.7	148.8	148.0	147.1	146.3	145.5	144.7	143.9
0.36	143.1	142.3	141.5	140.7	140.0	139.2	138.4	137.7	136.9	136.2
0.37	135.5	134.7	134.0	133.3	132.6	131.9	131.2	130.5	129.8	129.1
0.38	128.4	127.7	127.1	126.4	125.8	125.1	124.5	123.8	123.2	122.6
0.39	121.9	121.3	120.7	120.1	119.5	118.9	118.3	117.7	117.1	116.5
0.40	115.9	115.3	114.8	114.2	113.6	113.1	112.5	111.9	111.4	110.9
0.41	110.3	109.8	109.3	108.7	108.2	107.7	107.2	106.6	106.1	105.6
0.42	105.1	104.6	104.1	103.6	103.1	102.7	102.2	101.7	101.2	100.8
0.43	100.3	99.8	99.4	98.9	98.5	98.0	97.6	97.1	96.7	96.2
0.44	95.8	95.3	94.9	94.5	94.1	93.6	93.2	92.8	92.4	92.0
0.45	91.6	91.2	90.8	90.4	90.0	89.6	89.2	88.8	88.4	88.0
0.46	87.6	87.3	86.9	86.5	86.1	85.8	85.4	85.0	84.7	85.3
0.47	84.0	83.6	83.2	82.9	82.5	82.2	81.8	81.5	81.2	80.8
0.48	80.5	80.2	79.8	79.5	79.2	78.8	78.5	78.2	77.9	77.6
0.49	77.2	76.9	76.6	76.3	76.0	75.7	75.4	75.1	74.8	74.5
0.50	74.2	73.9	73.6	73.3	73.0	72.7	72.4	72.1	71.9	71.6
0.51	71.3	71.0	70.7	70.5	70.2	69.9	69.6	69.4	69.1	68.8
0.52	68.6	68.3	68.1	67.8	68.5	67.3	67.0	66.8	66.5	66.3
0.53	66.0	65.8	65.5	65.3	65.0	64.8	64.5	64.3	64.1	63.8
0.54	63.6	63.4	63.1	62.9	62.7	62.4	62.2	62.0	61.7	61.5

TABLE B.1: Extract of Vickers hardness conversion table (HV10)

Appendix C

Procedure for the confidence intervals computation

C.1 Hydrostatic weighting

The hydrostatic weighting method requires to weight the analysed samples two times; once in air and once in water. The measurements data of the two weightings are subjected to a certain spreading - especially large in the case of underwater measurements. Both of the tests imprecisions must thus be taken into account when computing the confidence intervals (CI) for $\rho_{a,rel}$. The following procedure was followed:

- Computation of the standard deviation SD for the two data samples of observed mass values $\{x_1, x_2, \dots, x_N\}$ with the formula below:

$$SD = \sqrt{\frac{\sum_{i=1}^N (x_i - \bar{x})^2}{N - 1}}$$

where N the sample size and \bar{x} is the mean of the observed values.

- Determination of the CI range at a 95 [%] confidence level for each data sample with the following formula:

$$CI = \bar{x} \pm 1.96 \frac{SD}{\sqrt{N}}$$

- Use of the mean values incremented by the extreme values of the CI for both W_a and W_w in the formula:

$$\rho_a = \frac{W_a}{W_a - W_w} \cdot \rho_w$$

so as to maximise the absolute value of the difference with \bar{x} . This difference is then equal to the CI half length for a 95 [%] confidence level.

C.2 Vickers hardness

Hardness measurements of a given sample are also prone to having a certain variability. CI must thus be computed to assess the method precision. The CI is first calculated for the data sample composed of the mean diagonals length of the indents. For this purpose, one follows the same two first steps as for the hydrostatic

weighting. The CI range is then multiplied by 800 to find the hardness's one. This is done in accordance with the observation that the maximal hardness variation for a change of 0.001 [mm] is 0.8 [HV] in table B.1 for $H_v < 147.1$ [HV].

Bibliography

- [1] 3D Systems Inc, *Direct metal printers: Metal Additive Manufacturing with the ProXTM DMP 3D printers*. 2016. URL: http://sintermedia.gkn.com/blog/the-advantages-of-https://www.3dsystems.com/sites/default/files/2017-01/3D-Systems_DMP_Tech_Specs_USEN_2017.01.23_WEB.pdf (visited on 13/04/2018).
- [2] Nesma T. Aboulkhair et al. 'On the formation of AlSi10Mg single tracks and layers in selective laser melting: Microstructure and nano-mechanical properties'. In: *Journal of Materials Processing Tech.* 230.Complete (2016), pp. 88–98.
- [3] Nesma T. Aboulkhair et al. 'Reducing porosity in AlSi10Mg parts processed by selective laser melting'. In: *Additive Manufacturing* 1-4 (2014). Inaugural Issue, pp. 77 –86. URL: <http://www.sciencedirect.com/science/article/pii/S2214860414000062>.
- [4] Nesma T. Aboulkhair et al. 'Selective laser melting of aluminum alloys'. In: *MRS Bulletin* 42.4 (2017), 311–319.
- [5] Nesma T. Aboulkhair et al. 'The microstructure and mechanical properties of selectively laser melted AlSi10Mg: The effect of a conventional T6-like heat treatment'. In: *Materials Science and Engineering: A* 667 (2016), pp. 139 –146. URL: <http://www.sciencedirect.com/science/article/pii/S0921509316304890>.
- [6] Erhard Brandl et al. 'Additive manufactured AlSi10Mg samples using Selective Laser Melting (SLM): Microstructure, high cycle fatigue, and fracture behavior'. In: *Materials & Design* 34 (2012), pp. 159 –169. URL: <http://www.sciencedirect.com/science/article/pii/S0261306911005590>.
- [7] John Daintith. *A Dictionary of Physics*. Oxford University Press, 2009. URL: <http://www.oxfordreference.com/view/10.1093/acref/9780199233991.001.0001/acref-9780199233991>.
- [8] Pauline Delroisse et al. 'Effect of strut orientation on the microstructure heterogeneities in AlSi10Mg lattices processed by selective laser melting'. In: *Scripta Materialia* 141 (2017), pp. 32 –35. ISSN: 1359-6462.
- [9] Christian Haase et al. 'Exploiting Process-Related Advantages of Selective Laser Melting for the Production of High-Manganese Steel.' In: *Materials* 10(1).56 (2017).
- [10] Simon Hoeges. *Additive manufacturing technologies: 6 Unique Benefits Of Selective Laser Melting*. 2017. URL: <http://sintermedia.gkn.com/blog/the-advantages-of-selective-laser-melting> (visited on 12/04/2018).
- [11] Frank I. Katch. 'Apparent Body Density and Variability during Underwater Weighing'. In: *Research Quarterly. American Association for Health, Physical Education and Recreation* 39.4 (1968), pp. 993–999. URL: <https://tandfonline.com/doi/abs/10.1080/10671188.1968.10613450>.

- [12] K. Kempen et al. 'Mechanical Properties of AlSi10Mg Produced by Selective Laser Melting'. In: *Physics Procedia* 39 (2012). Laser Assisted Net shape Engineering 7 (LANE 2012), pp. 439 –446. URL: <http://www.sciencedirect.com/science/article/pii/S1875389212025862>.
- [13] Karolien Kempen et al. 'Microstructural analysis and process optimization for selective laser melting of AlSi10Mg'. In: *Solid Freeform Fabrication Symposium Proceedings* (2011). Conference paper, pp. 484–495. URL: <https://sffsymposium.engr.utexas.edu/Manuscripts/2011/2011-37-Kempen.pdf>.
- [14] K.-H. Leitz et al. 'Multi-physical simulation of selective laser melting'. In: *Metal Powder Report* 72.5 (2017), pp. 331 –338. URL: <http://www.sciencedirect.com/science/article/pii/S0026065716300200>.
- [15] Xiao Peng Li et al. 'Tailoring Commercially Pure Titanium Using Mo2C During Selective Laser Melting'. In: *Solid Freeform Fabrication 2017: Proceedings of the 28th Annual International* (Aug. 2017). Conference paper, pp. 160–166.
- [16] Rene Lippert and Roland Lachmayer. 'A Design Method for SLM-Parts Using Internal Structures in an Extended Design Space'. In: (Sept. 2018), pp. 14–23.
- [17] Bochuan Liu et al. 'Investigaztion the effect of particle size distribution on processing parameters optimisation in selective laser melting process'. In: (Jan. 2011). Conference paper, pp. 227–238.
- [18] Anne I. Mertens, Jocelyn Delahaye and Jacqueline Lecomte-Beckers. 'Fusion-Based Additive Manufacturing for Processing Aluminum Alloys: State-of-the-Art and Challenges'. In: *Advanced Engineering Materials* 19.8 (2017), p. 1700003. URL: <https://onlinelibrary.wiley.com/doi/abs/10.1002/adem.201700003>.
- [19] Todd M. Mower and Michael J. Long. 'Mechanical behavior of additive manufactured, powder-bed laser-fused materials'. In: *Materials Science and Engineering: A* 651 (2016), pp. 198 –213. URL: <http://www.sciencedirect.com/science/article/pii/S092150931530530X>.
- [20] K.G. Prashanth, S. Scudino and J. Eckert. 'Defining the tensile properties of Al-12Si parts produced by selective laser melting'. In: *Acta Materialia* 126 (2017), pp. 25 –35. URL: <http://www.sciencedirect.com/science/article/pii/S135964541630982X>.
- [21] Noriko Read et al. 'Selective laser melting of AlSi10Mg alloy: Process optimisation and mechanical properties development'. In: *Materials & Design* (1980-2015) 65 (2015), pp. 417 –424. URL: <http://www.sciencedirect.com/science/article/pii/S0261306914007468>.
- [22] Renishaw plc, *AlSi10Mg-0403 powder for additive manufacturing data sheet*. 2015. URL: file:///E:/Downloads/H-5800-1061-01-A_AlSi10Mg-0403_400_W_material_data_sheet.pdf (visited on 15/04/2018).
- [23] Sartorius AG, *Sartorius BP121S Installation And Operating Instructions Manual*. 2000. URL: <https://www.manualslib.com/products/Sartorius-Bp121s-3748053.html> (visited on 15/04/2018).
- [24] Ming Tang, P. Chris Pistorius and Jack L. Beuth. 'Prediction of lack-of-fusion porosity for powder bed fusion'. In: *Additive Manufacturing* 14 (2017), pp. 39 –48. URL: <http://www.sciencedirect.com/science/article/pii/S2214860416300471>.

- [25] Naor Elad Uzan et al. 'Fatigue of AlSi10Mg specimens fabricated by additive manufacturing selective laser melting (AM-SLM)'. In: *Materials Science and Engineering: A* 704 (2017), pp. 229 –237. URL: <http://www.sciencedirect.com/science/article/pii/S0921509317310316>.
- [26] Robert C Weast. *CRC Handbook of Chemistry and Physics 53rd Edition*. CRC Press, 1973. URL: http://jupiter.plymouth.edu/~jsduncan/courses/2012_Spring/Techniques/Exams/DensityOfWater-vs-Temp.pdf.
- [27] Christian Weingarten et al. 'Formation and reduction of hydrogen porosity during selective laser melting of AlSi10Mg'. In: *Journal of Materials Processing Technology* 221 (2015), pp. 112 –120. URL: <http://www.sciencedirect.com/science/article/pii/S0924013615000564>.
- [28] Chor Yen Yap et al. 'Review of selective laser melting: Materials and applications'. In: 2 (Dec. 2015), p. 041101.
- [29] Yan Zhou et al. 'Investigation on the scan strategy and property of 316L stainless steel-Inconel 718 functionally graded materials fabricated by selective laser melting'. In: *The Proceedings of the 26th Solid Freeform Fabrication Symposium* (Aug. 2015). Conference paper, pp. 700–707.